ACS APPLIED ENERGY MATERIALS

www.acsaem.org Article

Room-Temperature Solid-State Lithium-Ion Battery Using a $LiBH_4$–MgO Composite Electrolyte

Valerio Gulino, Matteo Brighi, Fabrizio Murgia, Peter Ngene, Petra de Jongh, Radovan Černý, and Marcello Baricco*

Cite This: *ACS Appl. Energy Mater.* 2021, 4, 1228–1236 Read Online

ACCESS | Metrics & More | Article Recommendations | Supporting Information

ABSTRACT: $LiBH_4$ has been widely studied as a solid-state electrolyte in Li-ion batteries working at 120 °C due to the low ionic conductivity at room temperature. In this work, by mixing with MgO, the Li-ion conductivity of $LiBH_4$ has been improved. The optimum composition of the mixture is 53 v/v % of MgO, showing a Li-ion conductivity of 2.86×10^{-4} S cm^{-1} at 20 °C. The formation of the composite does not affect the electrochemical stability window, which is similar to that of pure $LiBH_4$ (about 2.2 V *vs* Li^+/Li). The mixture has been incorporated as the electrolyte in a TiS_2/Li all-solid-state Li-ion battery. A test at room temperature showed that only five cycles already resulted in cell failure. On the other hand, it was possible to form a stable solid electrolyte interphase by applying several charge/discharge cycles at 60 °C. Afterward, the battery worked at room temperature for up to 30 cycles with a capacity retention of about 80%.

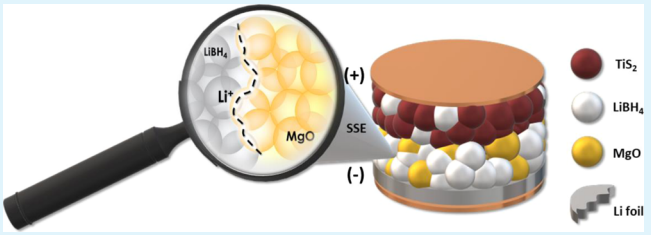

KEYWORDS: *complex hydride, solid-state electrolyte, all-solid-state Li-ion battery, lithium borohydride, solid electrolyte interface*

1. INTRODUCTION

Li-ion batteries (LIBs) are widely used in portable devices and play a major role in the fast-growing electro-mobility market. Solid-state electrolytes (SSEs) are promising candidates for resolving the intrinsic limitations of the organic liquid electrolyte currently employed in LIBs, such as the low cation transference number, the incompatibility (due to the uneven Li plating resulting in shortcuts) and reactivity with lithium metal anodes, and flammability.[1−3] Such drawbacks limit the cell energy density and require major safety precautions. SSEs can overcome these hindrances or bottleneck limitations, thanks to their intrinsic stiffness, which makes them less prone to dendrite penetration.[4] Moreover, superior chemical stability allows the use of metallic lithium as a negative electrode.[5,6] The improved safety naturally comes from the solid nature of the electrolyte. An SSE must fulfill several requirements to be employed in an all-solid-state battery (SSB), such as a Li-ion conductivity higher than 10^{-3} S cm^{-1} at room temperature (RT), a negligible electronic conductivity, and a wide electrochemical stability window.[3]

Different classes of materials have been proposed as SSEs, among which are complex hydrides.[1,7] Lithium borohydride ($LiBH_4$) has been extensively studied as an SSE, thanks to a remarkable ionic conductivity (σ) above 120 °C, combined with a low density (0.666 g/cm^3). In fact, the $LiBH_4$ RT-polymorph has an orthorhombic unit cell, space group (s.g.) *Pnma*, showing low Li-ion conductivity (10^{-8} S cm^{-1}), while around 110 °C,[8] it shows a polymorphic orthorhombic-to-hexagonal (s.g. $P6_3mc$) transition, rising the ionic conductivity of several orders of magnitude (~10^{-3} S cm^{-1} at 120 °C).[9] Recently, $LiBH_4$ has been reported to be electrochemically stable up to about 2 V *versus* Li^+/Li,[10,11] reducing the value of 5 V *versus* Li^+/Li previously overestimated.[12]

Halide substitution was adopted to enhance the RT Li^+ conductivity in $LiBH_4$. A solid solution is formed by substituting BH_4^- with I^-, Br^-, and Cl^-, stabilizing the hexagonal polymorph at RT.[10,13,14] Mixing other complex anions with $LiBH_4$ (*e.g.*, NH_2^- and NH^{2-}) leads to the formation of compounds with different structures, with enhanced ionic conductivity at RT.[15,16] Recently, it was reported that partial dehydrogenation of $LiBH_4$ leads to different Li−B−H complexes with significantly higher Li-ion conductivity (~2.7×10^{-4} S cm^{-1} at 35 °C).[17]

An alternative method to improve the Li-ion conductivity of the orthorhombic $LiBH_4$ (o-$LiBH_4$) is by nanoconfinement in suitable scaffolds or mixing it with oxides, forming oxide-based composites.[18−22] In this case, the improved Li-ion conductivity relies on the formation of a conductive interface, described by a core−shell model.[20,23] The fraction of $LiBH_4$ (the core) in direct contact with the oxide (the shell) forms an interfacial layer, featuring a Li-ion conductivity enhancement. The

Received: October 13, 2020
Accepted: January 15, 2021
Published: January 29, 2021

presence of different dynamics, due to the occurrence of slow and fast diffusivity of Li ions, has been detected for binary composites by ^{7}Li solid-state NMR spectroscopy.[22,24,25] The effective thickness of such an interfacial layer has been calculated by Suwarno *et al.*,[21] amounting to 1.94 ± 0.13 nm for a SiO_2 nanoscaffold. In the $LiBH_4$−SiO_2 system,[26] Li conductivity is optimized when $LiBH_4$ completely fills the silica pores with a thickness of the interfacial layer of about 2 nm, which is in good agreement with the results obtained by Suwarno.[21] Recently, Gulino *et al.*[26] reported two composite systems ($LiBH_4$−ZrO_2 and $LiBH_4$−MgO) that have shown improved RT conductivity (~10^{-4} S cm^{-1}) compared to *o*-$LiBH_4$. Liu *et al.*[27] reported that two-dimensional MoS_2 and $LiBH_4$ composites yielded an RT ionic conductivity of (~10^{-4} S cm^{-1}).

$LiBH_4$ was studied as an SSE in several SSBs[28] using TiS_2[29] or sulfur[30] as cathode materials. These SSBs operate at a temperature of about 120 °C, allowing a sufficiently high Li-ion conductivity due to the presence of the hexagonal polymorph of $LiBH_4$. The working potential of both TiS_2 and S is about 2 V *versus* Li^+/Li,[29,30] close to the electrochemical stability window of $LiBH_4$, which is one of the factors explaining the progressive capacity fading. In order to decrease the SSB-operating temperature, Unemoto *et al.*[31] used a $LiBH_4$−P_2S_5 mixture as the SSE, while Das *et al.*[32] reported an SSB working at 55 °C using $LiBH_4$ nanoconfined in silica (MCM-41) as the SSE.

Optimization of the composition of $LiBH_4$-based composites as an SSE can reduce the working temperature of the $LiBH_4$-based SSBs. Therefore, the aim of this work is to design a $LiBH_4$-based system as an improved SSE for RT SSBs. The $LiBH_4$−MgO system was selected, and the effect of the composition on the Li-ion conductivity was first established. The electrochemical stability window, measured by cyclic voltammetry (CV), was then determined in order to investigate the effect of the oxide matrix on the electrochemical stability of $LiBH_4$. A solid-state cell configuration, that is, TiS_2|SSE|Li, was selected as the electrochemical system, focusing on the characterization of the composite $LiBH_4$−MgO as the SSE for SSBs. These composites allowed to decrease the operating temperature of the $LiBH_4$-based SSB down to 60 °C and even down to RT, compared to the 120 °C of pure $LiBH_4$. Several cycles at 60 °C, and probably the concomitant formation of a stable solid electrolyte interphase, allowed us to successfully operate the SSB at RT for more than 30 cycles, with a discharge capacity retention of 80%.

2. EXPERIMENTAL SECTION

2.1. Synthesis. The Li-ion conductivity in the $LiBH_4$−MgO system has been evaluated for different compositions following the procedure suggested in ref 26. Three samples were synthetized, with a v/v % of MgO corresponding to a fraction of pore filling equal to 1/3, 1, and 3 (CE26, CE53, and CE74, respectively) assuming that $LiBH_4$ fills the pores of MgO after ball milling. $LiBH_4$ (purity > 95%, Alfa Aesar) was mixed with MgO (Steam Chemicals) in different ratios (Table 1).

In order to remove the physisorbed/chemisorbed water, MgO pellets were dried in a furnace for 6 h, under dynamic vacuum (by rotary pump), at 300 °C. Before the mechanochemical treatment for the preparation of the different compositions, the as-received $LiBH_4$ was ball-milled for 2 h at 500 rpm in a Fritsch Pulverisette 7 planetary mill and was used as the starting material for the $LiBH_4$−oxide composite. All samples were ball-milled for three periods of 10 min at 300 rpm, separated by 1 min breaks, in 80 mL stainless-steel vials, with stainless-steel spheres (10 mm diameter). The ball-to-sample mass ratio used was equal to 30:1. The mechanochemical treatment was performed under an argon atmosphere for all samples. Due to the air sensitivity of the samples, they have been manipulated in a glovebox (MBraun Lab Star Glove Box) filled with argon, with residual impurities (<1 ppm O_2 and <1 ppm H_2O).

Table 1. Composition, Fraction of the Pore Filled, and Thickness of $LiBH_4$ of Investigated Samples

sample name	oxide fraction (wt %)	oxide fraction (v/v %)	fraction of pore filled[a] (%)	thickness of $LiBH_4$[b] (nm)
26CE	65.0	26	323	3.8
53CE	85.7	53	100	1.2
74CE	94.0	74	38	0.4

[a]Data obtained from the ratio between the $LiBH_4$ volume per gram of MgO and the pore volume (V_p). [b]Thickness of the $LiBH_4$ layer covering the surface of the oxide (BET), assuming a uniform layer of $LiBH_4$ on the oxide surface.

2.2. Characterization. *2.2.1. Structural Characterization.* The density of MgO has been taken as 3.58 g/cm^3 from the literature.[33] The surface properties of MgO were analyzed by N_2 adsorption at 77 K in a TriStar Plus II gas-volumetric apparatus (Micromeritics, Norcross, GA, USA). The specific surface area (S_{BET}) was calculated by fitting the experimental data points with a Brunauer−Emmett−Teller isotherm[34] and was 215 m^2/g. The pore volume (V_p) was derived from the volume of absorbed nitrogen at p/p_0 = 0.95 and was 0.25 cm^3/g. Powder X-ray diffraction (PXRD) analysis has been performed on the as-prepared composites, see the Supporting Information.

2.2.2. Electrochemical Impedance Spectroscopy. Li-ion conductivity data for the samples were obtained by collecting the electrochemical impedance spectroscopy (EIS) spectra following the procedure reported in ref 10. The EIS measurements were performed using an HP4192A LF impedance analyzer and a Novocontrol (BDS 1200) sample cell in the temperature range of 20 < *T* < 130 °C (every 10 °C). By using an axial hydraulic press (60 MPa), the mixtures were pelletized, with a diameter of 10 mm and a thickness of about 0.2−0.6 mm. Impedance data were analyzed via the EqC software[35] following the data validation described in ref 36. All fits performed resulted in a χ-squared test (χ^2 test) < 10^{-3}.

2.2.3. Cyclic Voltammetry. CV was used to analyze the oxidative limit of the electrochemical stability window. The desired $LiBH_4$−MgO composite was mixed with carbon black (CB, Ketjenblack EC600JD, Akzo Nobel Chemicals) in a weight ratio of 95:5 using an agate mortar.[11] A two-layered pellet was obtained by pressing the 8 mg CE-composite mixture and about 25 mg of the composite at 240 MPa using a uniaxial hydraulic press (diameter 6 mm). The pellet thus prepared was tested in a two-electrode 3/4″ PTFE Swagelok-type cell, with a lithium disk (99.9%, Sigma-Aldrich) as the counter and reference electrode (SSE side) and a stainless-steel disk as the working electrode (SSE + CB side). The cells were tested with a potentiostat/galvanostat Biologic MPG-2 after a 4 h rest at 60 °C. CV measurements have been performed into a 1.3 < *V* < 5 V *versus* Li^+/Li voltage region at a scanning rate of 20 μV s^{-1}.

2.2.4. Battery Assembly and the Electrochemical Test. TiS_2 (99.9%, Sigma-Aldrich) was selected as the active material for the cathode. The TiS_2 and $LiBH_4$ powders were mixed in an agate mortar using a 1:1 weight ratio. The resulting mixture was used as the positive electrode. A two-layered pellet was prepared with 2 mg of the positive electrode mixture and 25 mg of the SSE by cold pressing at 240 MPa using a uniaxial hydraulic press (diameter 6 mm). A pure lithium disk was used as the negative electrode. The assembled bulk-type TiS_2/SSE/Li SSB was placed in a 3/4″ PTFE Swagelok-type cell. The galvanostatic cycling was performed in the voltage range of 1.7−2.5 V at 60 °C and at RT. EIS measurements were also performed in the symmetric configuration Li/SSE/Li and on the TiS_2/SSE/Li SSB

https://dx.doi.org/10.1021/acsaem.0c02525
ACS Appl. Energy Mater. 2021, 4, 1228−1236

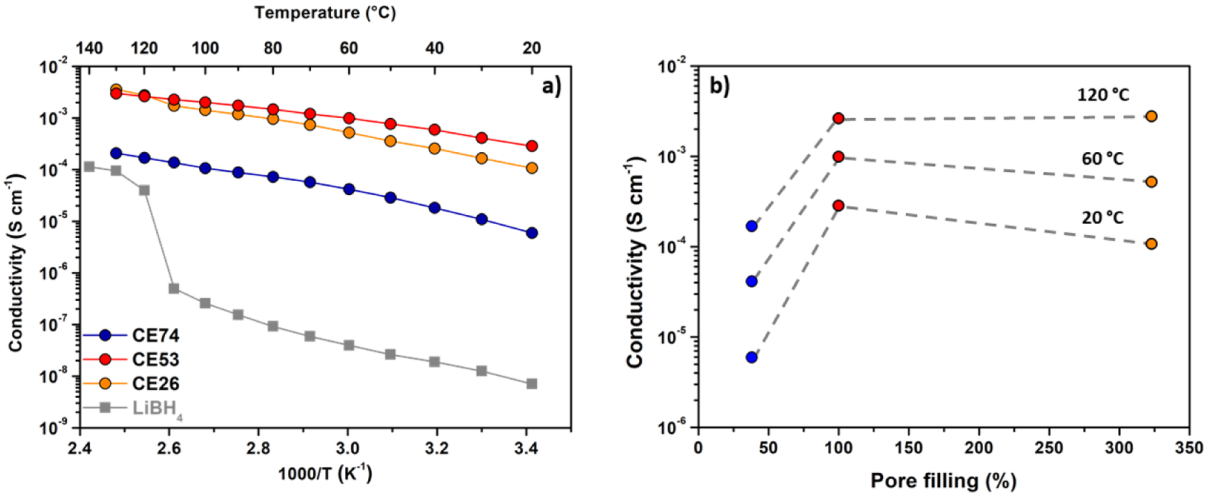

Figure 1. (a) Li-ion conductivity, obtained from a temperature-dependent EIS cycle during the second heating, for $LiBH_4$−MgO composites with different oxide fractions. The gray line corresponds to the Li-ion conductivity of pure $LiBH_4$.[10] (b) Li-ion conductivity at 20, 60, and 120 °C as a function of the pore filling. Dashed lines are a guide for the eyes.

during the rest time, before the battery cycling, and after each discharge and charge.

3. RESULTS AND DISCUSSION

3.1. Tailoring of the $LiBH_4$−MgO Composition. The AC conductivity of the composites as a function of the inverse temperature is shown in Figure 1a. The 20 °C impedance spectra (composed by a single arc and a low-frequency linear dispersion) are plotted together in the Nyquist plot in Figure S1, and the EIS-fitted values are reported in Table S1.

Figure 1a shows that at RT, sample CE53 shows the highest Li-ion conductivity (2.86×10^{-4} S cm^{-1} at 20 °C), about 4 orders of magnitude higher than that of pure $LiBH_4$. The 20 °C Li-ion conductivities of CE26 and CE74 were 1.07×10^{-4} and 5.94×10^{-6} S cm^{-1}, respectively. The Li-ion conductivity of sample CE26 at 40 °C (2.57×10^{-4} S cm^{-1}) is in agreement with the data already reported for the same composition and at the same temperature (1.80×10^{-4} S cm^{-1}).[26] The improved Li-ion conductivity likely relies on the formation of a conductive interface, described by a core−shell model.[20] It was demonstrated, by solid-state NMR, that the interface layer between $LiBH_4$ and silica is characterized by a high ion dynamics, for both BH_4^- and Li^+, and cannot be defined with a clear crystal structure.[37] The exact relation between the interface layer structure and the dynamics of ions needs further investigation.

The dependence on the pore filling of the Li conductivity at various temperatures is shown in Figure 1b, assuming that $LiBH_4$ completely fills the pore of the oxide during the mechanochemical treatment. The maximum σ value is observed for a 100% pore volume filling (Figure 1b), confirming the trend previously reported by Gulino *et al.*[26]

In order to explore the phase composition of the different composite, after synthesis, the PXRD patterns were collected (Figure S2). Orthorhombic $LiBH_4$ was detected only for sample CE26, that is, for a pore filling higher than 100%, indicating that the excess of hydride contained in this composite is partially present as the RT polymorph.

From the trend of data reported in Figure 1a, it is worth noting that different conductive regimes are likely present, indicating a complex temperature-dependent Li-ion conduction mechanism in the investigated temperature range. This type of behavior has been previously reported for complex hydrides,[38] as well as for different classes of materials studied as SSEs,[39] and can be assigned to different ion−ion interaction regimes. Further investigation, that is, combining solid-state NMR and large frequency and temperature-range EIS measurements,[38,40] is needed in order to clarify this aspect.

The activation energy for the CE53 sample was obtained by fitting linearly ($R^2 > 0.999$) the $\ln(\sigma T)$ *versus* $1/T$ data shown in Figure 1a below 60 °C, where data suggest an Arrhenius-type temperature dependence. The so-obtained E_a is equal to 0.29 ± 0.03 eV below 60 °C. The obtained E_a is considerably lower than the average value reported in the literature for pure $LiBH_4$ (0.75 ± 0.07 eV),[41] but it is similar to values observed for other SSEs.[42]

For sample CE74, the pore-filling fraction is lower than 100%; therefore, the highly conductive phase does not percolate throughout the sample and the conductive pathway is interrupted by the oxide. A similar effect occurs in sample CE26, where the excess of the low conductive orthorhombic $LiBH_4$ interrupts the conductive pathway.

For the CE53 sample, the Li-ion conductivity is about 1 order of magnitude higher than the values previously reported for $LiBH_4$−SiO_2-based composite SSEs: at 40 °C Blanchard *et al.* obtained 1.0×10^{-5} S cm^{-1} for 28 v/v % of MCM-41,[20] Choi *et al.* obtained 1.5×10^{-5} S cm^{-1} for 55 v/v % of fumed silica,[19] and Gulino *et al.* obtained 4.1×10^{-5} S cm^{-1} for 20 v/v % of SiO_2.[26]

The Li-ion conductivity of CE74 and CE53 composites does not show, at 110 °C, the typical step due to the phase transition of $LiBH_4$, which is slightly visible for the CE26 sample (see also Figure S3). This suggests that the contribution of the hexagonal phase of $LiBH_4$ is negligible in the CE74 and CE53 samples at high temperatures, whereas it is relevant for the CE26 sample.[26] This behavior can be explained by assuming a homogeneous distribution of the $LiBH_4$ layer on MgO, as reported in our previous work,[26] providing estimated values for the interface layer thickness (see Table 1), which are similar to that obtained by Suwarno *et al.*[21]

The highly conductive layer of $LiBH_4$ in direct contact with the oxide, whose thickness has been estimated to be about 2 nm, does not undergo a structural phase transition.[21,26] Indeed, for samples CE74 and CE53, the calculated thicknesses of

https://dx.doi.org/10.1021/acsaem.0c02525
ACS Appl. Energy Mater. 2021, 4, 1228−1236

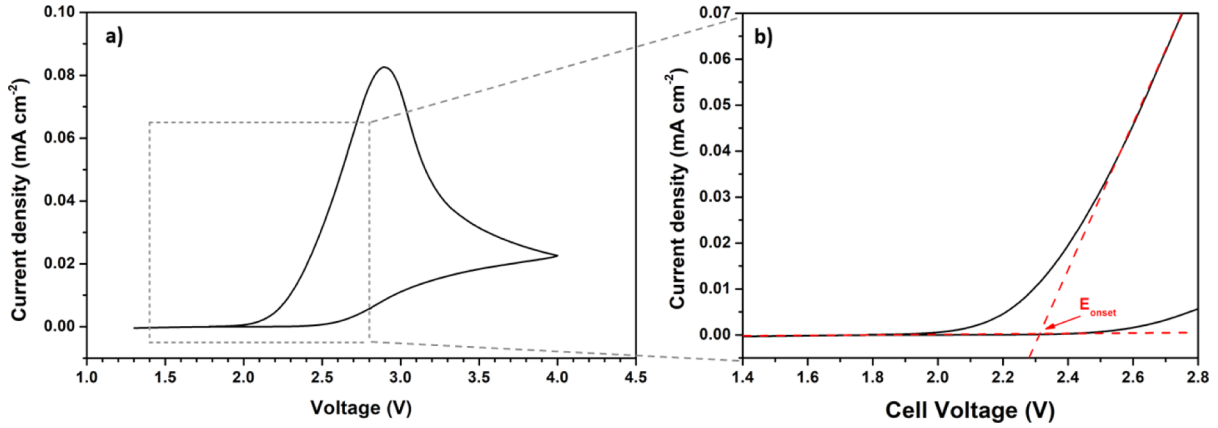

Figure 2. (a) Linear sweep voltammograms of Li|CE53|CE53-C|stainless-steel cells at a scan rate of 20 μV s^{-1} from 1.3 to 4.0 V *vs* Li$^+$/Li at 60 °C. (b) E_{onset} estimation from two linear regression lines of the nonfaradaic background current and faradaic anodic current.

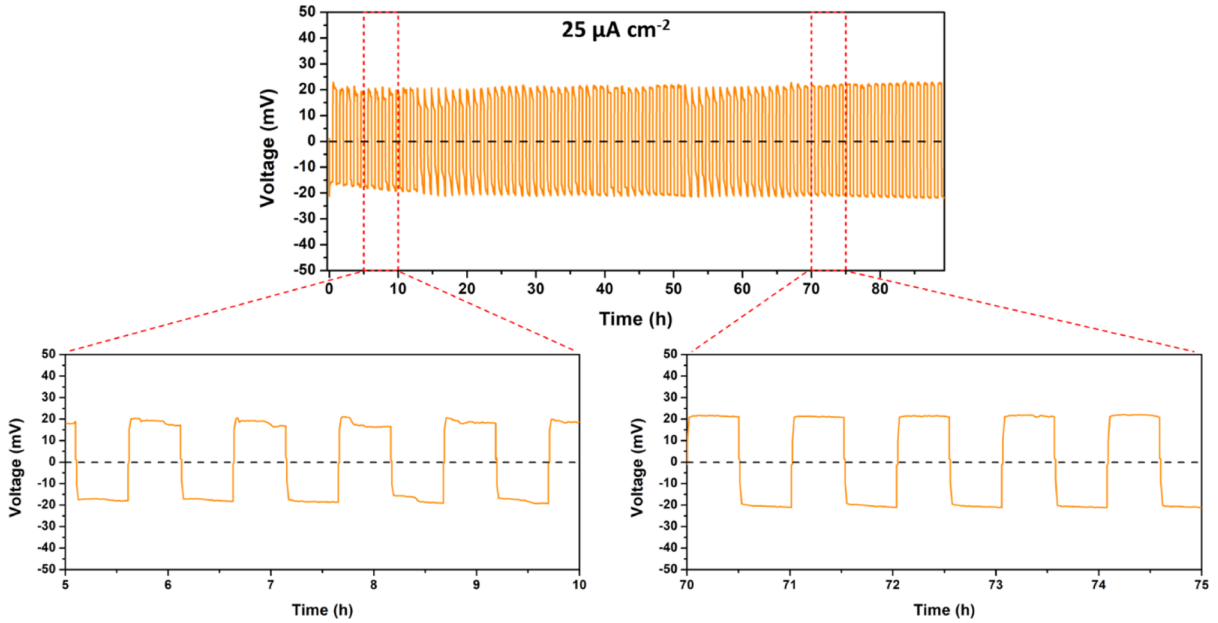

Figure 3. Galvanostatic cycling profiles of the symmetrical Li|CE53|Li cell at 60 °C with a current density of 25 μA cm^{-2} for 30 min sweeps.

$LiBH_4$ are 0.4 and 1.2 nm, respectively (see Table 1), which are close to the values estimated in the literature.[21,26] On the other hand, the calculated thickness of $LiBH_4$ for composite CE26 amounts to 3.8 nm, explaining the slight increase of the Li-ion conductivity above 110 °C (Figure 1a) and confirming that the bulk $LiBH_4$ contributes to the Li-ion conductivity after the phase transition.

3.2. Electrochemical Stability. Next to a high Li-ion conductivity, a suitable SSE should have a wide electrochemical stability window and a good chemical compatibility with electrodes. The electrochemical stability of the CE53 sample has been evaluated by CV at 60 °C (Figure 2a). The interface between a solid electrolyte pellet and a flat metallic Au working electrode can result in a low contact surface area and thus a high interface resistance, which can cause difficulty in the signal detection, for example, overestimating the electrochemical stability window. Therefore, in order to increase the probed surface, a carbon material was added, as described elsewhere.[43,44]

The oxidative limit (E_{onset}) was determined from the intersection of two linear regression lines (R^2 > 0.99) of the background current and the faradaic oxidative current at a positive potential *versus* Li$^+$/Li (Figure 2b) following the approach suggested by Asakura *et al.*[11] It falls at about 2.3 V *versus* Li$^+$/Li, which is in agreement with the values reported for $LiBH_4$ by Asakura *et al.*[11] and Gulino *et al.*[10] This result suggests that the addition of the MgO matrix only affects the ionic conductivity, leaving the electrochemical stability of $LiBH_4$ unchanged.

The chemical compatibility toward metallic lithium was evaluated with galvanostatic cycling in a Li|CE53|Li symmetrical cell at 60 °C, allowing to also determine the extent of the reversible lithium plating/stripping at the SSE surface and, at the same time, its reductive stability. The results, shown in Figure 3, demonstrate that lithium is plated and stripped reversibly for over 90 h.

The cell polarization is rather steady at 20 mV for the whole period, indicating a long-term stability and that no parasitic reactions between the SSE and lithium occur in this low potential region. Indeed, a well-performing electrochemical material should show a stable polarization, reflecting the electrolyte resistivity and interfacial effects, in case they are

https://dx.doi.org/10.1021/acsaem.0c02525
ACS Appl. Energy Mater. 2021, 4, 1228−1236

present. $LiBH_4$ has been already reported to be able to plat/strip lithium for a longer time and at higher current densities.[17,45]

The contact resistance of the cell was calculated by multiplying the cell resistance (after having subtracted the SSE contribution), divided by a factor of 2 (since the two interfaces are considered equivalent), by the contact surface. It turns out to be about 565 Ω cm^2, a much higher value than that reported by Kim *et al.*[46] on carborane SSEs (<1 Ω cm^2). In the absence of a proper cell stack pressure, which would guarantee an intimate contact between lithium and the SSE surfaces, a high contact resistance, increasing during cycling, is expected,[47,48] explaining the observed value.

3.3. Battery Test. The electrochemical properties of the CE53 composite SSE were tested in an SSB, selecting TiS_2 and Li as positive and negative electrodes, respectively. Lithium increases the energy density with respect to the commercial graphitic anodes,[4] while TiS_2 is widely used for $LiBH_4$-based SSBs.[29] In the current study, TiS_2 has also been selected to obtain a valid comparison with the system reported by Unemoto *et al.*[29]

The Li-ion conductivity of CE53 at 20 °C amounts to 2.86 × 10^{-4} S cm^{-1} and it is sufficient to operate the battery at RT at low current regimes.[3] Therefore, a freshly prepared cell was built and cycled at RT, without any conditioning. Figure 4 depicts the galvanostatic cycling with a potential limitation (GCPL) profile of the Li|CE53|TiS_2 cell, operating with a current density of 24 mA g^{-1} (C/10).

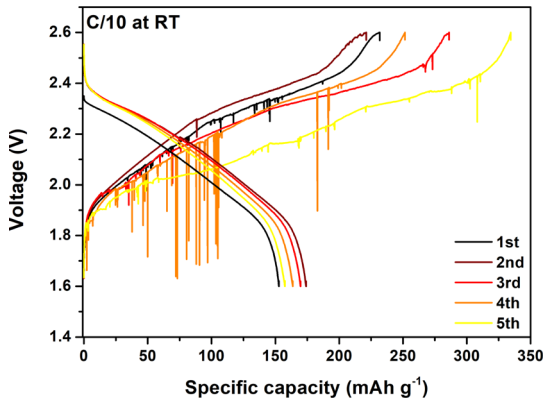

Figure 4. Voltage profiles of the Li|CE53|TiS cell for a rate of C/10 (*i.e.*, 24 mA/g) at RT.

Figure 4 shows that it was possible to collect data for only five cycles before the cell failure and several spikes are visible in the charge profiles, but they are completely missing during discharges. These results suggest an inhomogeneous Li plating and it may be induced by the imposition of a current density exceeding the so-called critical current density,[49,50] which is also a function of the cell stack pressure.[48]

A significant difference between the discharge capacity at the first and the second cycle (52 and 173 mA h g^{-1}, respectively) has been observed. Unemoto *et al.*[29] observed a similar behavior for the Li|$LiBH_4$|TiS_2 battery, operating at 120 °C. By probing the evolution of $LiBH_4$ into $Li_2B_{12}H_{12}$, it has been related to a partial instability of the TiS_2/$LiBH_4$ interface, forming H_2 and additional Li, that self-diffuses into TiS_2, self-discharging the battery.[29] The recently reported value of 2.2/2.3 V *versus* Li^+/Li for the electrochemical window of $LiBH_4$ clarifies that the TiS_2/$LiBH_4$ interfacial instability arises when the $LiBH_4$ oxidation potential is exceeded.[10,11] In the present case, the self-discharging reaction to form a solid electrolyte interface (SEI), as evidenced by the capacity difference between the first and the second cycle, is much less extended than that reported by Unemoto *et al.*[29] (*i.e.*, discharge capacities of 80 and 205 mA h g^{-1} for the first and second cycles, respectively). This is probably due to a kinetic limitation in the reaction of $LiBH_4$ to form likely $Li_2B_{12}H_{12}$ as a consequence of the lower temperature.

In order to gain further insights into the effect of the temperature on the formation of the SEI, a freshly prepared cell was built and cycled at 60 °C. Figure 5a shows the GCPL profile of the Li|CE53|TiS_2 cell operating at 60 °C and with a current density of 11.8 mA g^{-1} (corresponding to C/20).

For the sake of clarity, only selected galvanostatic profiles are shown. A high capacity retention was observed over 65 cycles when the battery operated at 60 °C. A rather low discharge capacity has been observed at the first cycle (101 mA h g^{-1}). On the other hand, its value at the second cycle amounts to 175 mA h g^{-1} that corresponds to about 73% of the theoretical capacity of TiS_2 (239 mA h g^{-1}).[51,52]

The self-discharge due to the formation of the $Li_2B_{12}H_{12}$ SEI is also observed in this case but with a higher extent with respect to the test performed at RT (Figure 4). The higher self-discharge observed is consistent with a faster kinetics of the reaction of $LiBH_4$ to form $Li_2B_{12}H_{12}$, which is favored by the higher temperature.

Figure 5b shows the discharge/charge capacity, Coulombic efficiency, and discharge capacity retention ratio to the second discharge as a function of cycle number. The capacity retention has been calculated with respect to the second discharge capacity since in the first run the capacity is overestimated due to the self-discharge reaction occurring at the TiS_2/$LiBH_4$ interface. The discharge capacity retention is more than 80% after 65 cycles, which is promising for a stable battery operation at this temperature.

It is worth noting that after the 30th cycle (Figure 5a), a pronounced decrease of the capacity is observed (*i.e.*, discharge capacities of 174, 147, and 139 mA h g^{-1} for the 2nd, the 30th, and the 65th cycle, respectively). On the other hand, the Coulombic efficiency is always close to 99.9% up to the 10th cycle (Figure 5b), indicating that the capacity fading occurs during the charge, namely, at a voltage higher than the oxidative stability of $LiBH_4$.

To clarify the cause of this effect, the cell impedance was monitored after each charge/discharge cycle and results are reported in Figure S4 in the Supporting Information. The contact resistance (R_1), at the very first discharge, is <1 Ω (similar to that obtained by Kim *et al.*),[46] and afterward, it quickly increases in the first 10 cycles and then reaches a steady exponential increase. This behavior can be understood considering the sum of two contributions. The first one is the formation of the $Li_2B_{12}H_{12}$-based SEI layer, that is, poor conductivity at 60 °C (lower than 10^{-6} S cm^{-1}).[53] The decrease of the capacity fading at the 30th cycle could correspond to the achievement of the maximal SEI thickness. The second contribution, being the cell not supported by an appropriate stack pressure, is likely due to a continuous loss of contact at the electrode interfaces. In fact, during the delithiation of TiS_2, a volume contraction of $\Delta V/V = -9.7\%$ is experienced, which also explains the rather high contact resistance after each charge cycle (Figure S4 in the Supporting

https://dx.doi.org/10.1021/acsaem.0c02525
ACS Appl. Energy Mater. 2021, 4, 1228−1236

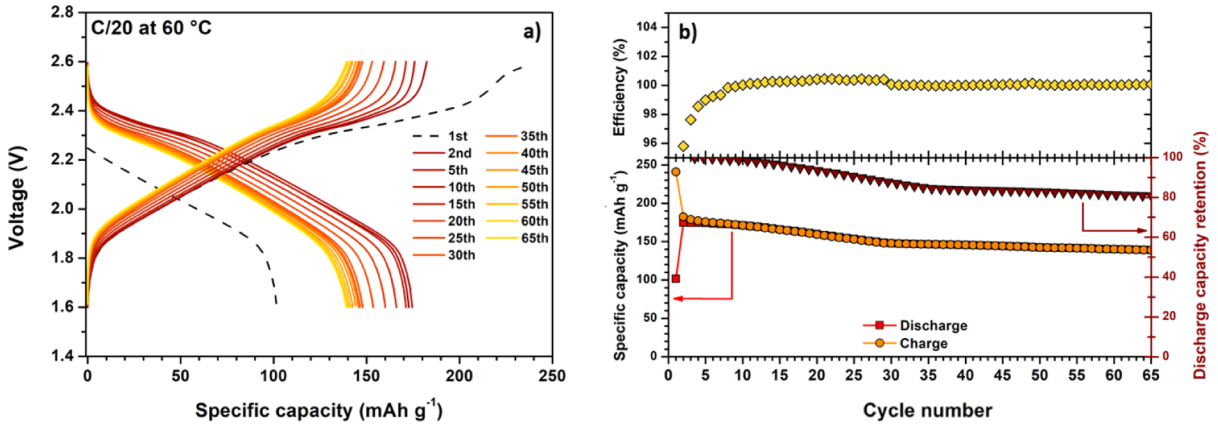

Figure 5. (a) Voltage profiles of the Li|CE53|TiS_2 cell for a rate of C/20 (11.8 mA g^{-1}) at 60 °C. (b) Discharge/charge specific capacity, Coulombic efficiency (discharge capacity over charge capacity), and discharge capacity retention ratio as a function of cycle number for the same cell. The capacity of the battery is expressed per gram of TiS_2.

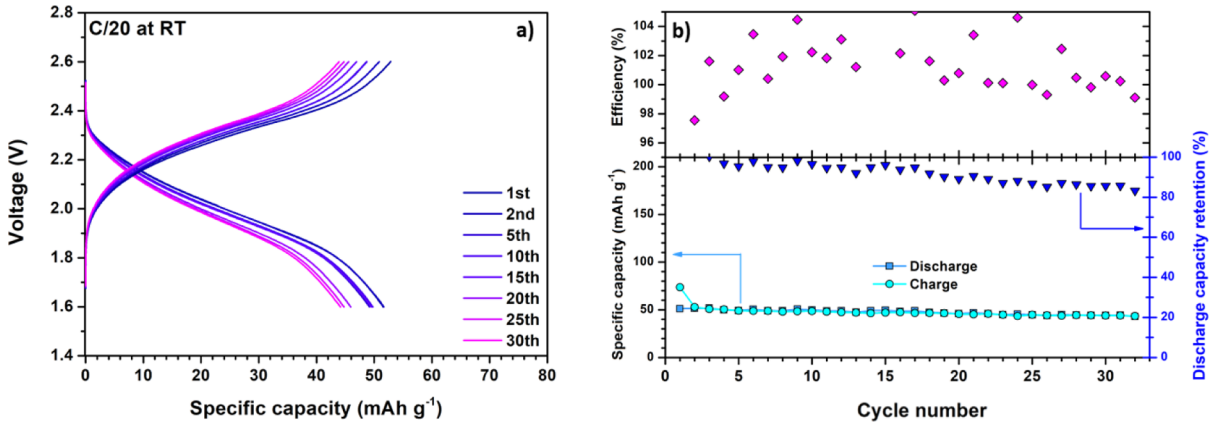

Figure 6. (a) Voltage profiles of the Li|CE53|TiS_2 cell for a rate of C/20 at RT after 65 cycles at 60 °C at the C/20 rate. (b) Discharge/charge specific capacity, Coulombic efficiency (discharge capacity over charge capacity), and discharge capacity retention ratio (to the second discharge capacity) as a function of cycle number for the same cell.

Information), that is, after Li plating at the negative electrode. The Li_xTiS_2 $\Delta V/V$ value was estimated assuming a complete deintercalation; so, considering the unit cell volume at the two intercalation extremes, $x = 0$ and at $x = 1$. In addition, when considering the negative side of the cell, a similar trend of the contact resistance has been reported by Krauskopf *et al.*,[54] when the current density is higher than a critical value (*i.e.*, 200 μA cm^{-1} at RT) without a suitable external applied pressure. Therefore, we assume that the contact degradation happens at both the cathode and anode and that it is the main reason of the capacity fading after the 30th cycle.

In order to investigate a possible dependence of SEI formation from the amount of $LiBH_4$ in the SSE, that is, from the $LiBH_4$/MgO volume ratio, a similar cell was built using the CE26 composite as the electrolyte. Figure S5 in the Supporting Information shows the GCPL profile of Li|CE26|TiS_2 at 60 °C, with a current density of 4.8 mA g^{-1} (corresponding to C/50). Also, in this case, the capacity obtained on the second cycle (176 mA h g^{-1}) is higher compared to that observed for the first one (82 mA h g^{-1}), confirming the occurrence of a self-discharge reaction, as described above. Interestingly, when comparing the properties of cells with CE26 and CE53 as SSEs, the same behavior is observed, that is, a stabilization of the capacity fading after a certain number of cycles. In this case, the change is observed at the 58th cycle, a time-shift that can likely be due to the slower kinetics imposed by lower current rates (C/50 instead of C/20).

The high Li-ion conductivity of the CE53 composite and the formation of an SEI at a high temperature allow the battery to operate at RT. Therefore, after 65 cycles performed at 60 °C, the temperature of the test for the Li|CE53|TiS_2 cell decreased to RT. A 4 h rest has been applied in order to equilibrate the temperature. Figure 6a shows the galvanostatic profiles using the same current density of 11.8 mA g^{-1} (C/20). For the sake of clarity, only selected galvanostatic profiles are shown.

Figure 6b shows the discharge/charge capacity, Coulombic efficiency, and capacity retention ratio to the second discharge as a function of cycle number. It is worth noting that the battery successfully operates at RT for more than 30 cycles, with a discharge capacity retention of 80%.

The capacity of the Li|CE26|TiS_2 cell at RT for the first cycle is 51 mA h g^{-1} (Figure 6), compared with the value of 139 mA h g^{-1} obtained for the 65th cycle at 60 °C. In order to clarify this difference, Figure S6 in the Supporting Information shows the voltage profiles of the 65th charge and discharge cycles shown in Figure 5 compared with those corresponding to the 1st cycle at RT (Figure 6). It is clear that the decrease of the working temperature causes an increase of the cell polarization, indicating that the capacity drop (*i.e.*, between the last cycle at 60 °C and the first cycle at RT) can be assigned to kinetic

https://dx.doi.org/10.1021/acsaem.0c02525
ACS Appl. Energy Mater. 2021, 4, 1228−1236

limitations due to the low temperature. During the 4 h rest, the evolution of the cell resistance was monitored by means of *in situ* EIS (Figure S7a in the Supporting Information). The increase of the cell resistance during the 4 h rest at RT is mainly related to the decrease of the ionic conductivity of the SSE. Figure S7b in the Supporting Information shows the contact resistance (R_1) after each charge discharge cycle at RT. Assuming that the formation of the SEI was completed during the first cycles at 60 °C, the steady increase of R_1 can be assigned to just a continuous contact loss, as also observed after the 30th cycle at 60 °C (Figure S4b in the Supporting Information). Despite this, CE53 allowed to operate the Li|CE53|TiS_2 system at RT, once the SEI was formed.

Comparing the behavior of the battery previously conditioned at 60 °C with respect to that operating directly at RT (Figure 4), it is evident that the high-temperature treatment stabilizes the interface by forming a stable interface compound such as the $Li_2B_{12}H_{12}$-based SEI, as suggested by Unemoto *et al.*,[29] allowing the cell to operate at RT. The longer life cycle suggests the prevention of electrolyte decomposition.

As mentioned above, Unemoto *et al.*[29] reported results on an SSB very similar to that investigated in the present study but using pure $LiBH_4$ instead of a composite as the SSE and operating at 120 °C since h-$LiBH_4$ was necessary to achieve the high Li-ion conductivity. The obtained capacity retention was 88% after 300 cycles at a C/5 rate. It has been reported that the higher working temperature increases the Li diffusion,[54,55] strongly limiting the void formation at the electrode interface during the stripping process. This effect limits the contact resistance evolution, significantly reducing the capacity fading, as observed by Unemoto *et al.*[29] even in the absence of an appropriate stack pressure, unlike the reported case at 60 °C. In contrast, the results reported here show that a drastical decrease of the operating temperature (*i.e.*, from 120 °C to RT) is possible, thanks to a $LiBH_4$−MgO nanocomposite as the solid electrolyte and the formation, at 60 °C, of a stable SEI. It is the first time that the formation of a stable SEI at a temperature (60 °C) higher than the operating one (RT) is applied to a hydride solid electrolyte and it is probably also relevant for other SSEs working in full solid-state LIBs, as already reported by Rodrigues *et al.*[56]

Clearly, optimization of the battery, to realize a long cycle-life SSB, would lead to a different electrode choice. For instance, elemental sulfur, which has a high theoretical capacity (1672 mA h g^{-1})[57] and a redox potential of ∼2.2 V, similar to the oxidative limit of the $LiBH_4$ electrochemical window (*i.e.*, 2.2 V *vs* Li^+/Li), would be a suitable electrode, possibly adopting an infiltration procedure for the electrode preparation, that is, dissolving the SSE in an opportune solvent and crystallizing it directly on the cathode material.[58,59] In addition, the optimization of the external cell stack pressure, recently suggested to be rather small (*i.e.*, 5 MPa),[60] would reduce the contact resistance, leading to a lower capacity fading.[47,54]

Finally, the cost of solid electrolyte materials is important, as well as effective large-scale production. The U.S. Department of Energy's Advanced Research Projects Agency-Energy (ARPA-E) has adopted an ambitious target of 10 $/$m^2$ for the cost area of solid electrolyte materials,[61,62] considering a 10 μm thickness. The SSE synthetized in this work is composed by easily available raw materials making the cost less than 2 $/g, corresponding to about 80 $/$m^2$. Considering that the up-scaling might decrease the cost, $LiBH_4$-based composites could be considered as competitive candidates to be used in Li-ion SSBs.

4. CONCLUSIONS

In this work, fast ionic conductors in the solid state, based on the $LiBH_4$−MgO system, were investigated. The samples were mechanochemically synthetized. The Li-ion conductivity of $LiBH_4$ was improved in all cases, and the samples containing 53 v/v % of MgO showed the best enhancement (2.86×10^{-4} S cm^{-1} at 20 °C), since the volume fraction of $LiBH_4$ allowed to completely fill the pore volume of MgO. The formation of a highly conductive layer does not affect the electrochemical stability window, which is similar to that of pure $LiBH_4$ (*i.e.*, about 2.2 V *vs* Li^+/Li).

A test at RT in a TiS_2/Li SSB allowed only five cycles before the cell failure. From a battery test at 60 °C, the incorporation of the solid electrolyte in the battery showed that a stable SEI is formed during the first charge/discharge cycles, causing an initial increase in contact resistance but limiting a further decomposition of the composite electrolyte. Afterward, the battery worked at RT for up to 30 cycles, with a specific capacity of about 50 mA h g^{-1}.

In conclusion, it has been demonstrated that the SEI, formed at 60 °C, allowed to reduce the operating temperature of the SSB down to RT. Therefore, a possible novel strategy to obtain an SSB working at RT, using complex hydrides as electrolytes, can be established by the formation of a stable SEI at higher temperatures. Despite this proof-of-concept, further optimization is mandatory to obtain an efficient battery (*e.g.*, electrode choice and casting and cell stack pressure).

■ ASSOCIATED CONTENT

Supporting Information

The Supporting Information is available free of charge at https://pubs.acs.org/doi/10.1021/acsaem.0c02525.

PXRD patterns, Nyquist plot with the fitting values, *in situ* EIS measurements of Li|CE53|TiS_2 working at 60 °C and RT, and GCPL profile of the Li|CE26|TiS_2 cell working at 60 °C (PDF)

■ AUTHOR INFORMATION

Corresponding Author

Marcello Baricco − *Department of Chemistry and Interdepartmental Center Nanostructured Interfaces and Surfaces (NIS), University of Turin, 10125 Torino, Italy;* orcid.org/0000-0002-2856-9894; Phone: +39 011 6707569; Email: marcello.baricco@unito.it; Fax: +39 0116707856

Authors

Valerio Gulino − *Department of Chemistry and Interdepartmental Center Nanostructured Interfaces and Surfaces (NIS), University of Turin, 10125 Torino, Italy; Inorganic Chemistry and Catalysis, Debye Institute for Nanomaterials Science, Utrecht University, 3584 CG Utrecht, The Netherlands;* orcid.org/0000-0002-5808-7802

Matteo Brighi − *Laboratoire de Cristallographie, DQMP, Université de Genève, CH-1211 Geneva 4, Switzerland*

Fabrizio Murgia − *Laboratoire de Cristallographie, DQMP, Université de Genève, CH-1211 Geneva 4, Switzerland*

Peter Ngene − *Inorganic Chemistry and Catalysis, Debye Institute for Nanomaterials Science, Utrecht University, 3584*

https://dx.doi.org/10.1021/acsaem.0c02525
ACS Appl. Energy Mater. 2021, 4, 1228−1236

CG Utrecht, The Netherlands; orcid.org/0000-0003-3691-0623

Petra de Jongh − *Inorganic Chemistry and Catalysis, Debye Institute for Nanomaterials Science, Utrecht University, 3584 CG Utrecht, The Netherlands;* orcid.org/0000-0002-2216-2620

Radovan Černý − *Laboratoire de Cristallographie, DQMP, Université de Genève, CH-1211 Geneva 4, Switzerland;* orcid.org/0000-0002-9847-4372

Complete contact information is available at: https://pubs.acs.org/10.1021/acsaem.0c02525

Notes

The authors declare no competing financial interest.

■ ACKNOWLEDGMENTS

Financial support from the Netherlands Organisation for Scientific Research (NWO-ECHO) is gratefully acknowledged.

■ REFERENCES

(1) Bachman, J. C.; Muy, S.; Grimaud, A.; Chang, H.-H.; Pour, N.; Lux, S. F.; Paschos, O.; Maglia, F.; Lupart, S.; Lamp, P.; Giordano, L.; Shao-Horn, Y. Inorganic Solid-State Electrolytes for Lithium Batteries: Mechanisms and Properties Governing Ion Conduction. *Chem. Rev.* **2016**, *116*, 140−162.

(2) Manthiram, A.; Yu, X.; Wang, S. Lithium Battery Chemistries Enabled by Solid-State Electrolytes. *Nat. Rev. Mater.* **2017**, *2*, 16103.

(3) Goodenough, J. B.; Kim, Y. Challenges for Rechargeable Li Batteries. *Chem. Mater.* **2010**, *22*, 587−603.

(4) Goodenough, J. B.; Singh, P. Review-Solid Electrolytes in Rechargeable Electrochemical Cells. *J. Electrochem. Soc.* **2015**, *162*, A2387−A2392.

(5) Culver, S. P.; Koerver, R.; Krauskopf, T.; Zeier, W. G. Designing Ionic Conductors: The Interplay between Structural Phenomena and Interfaces in Thiophosphate-Based Solid-State Batteries. *Chem. Mater.* **2018**, *30*, 4179−4192.

(6) Muldoon, J.; Bucur, C. B.; Gregory, T. Quest for Nonaqueous Multivalent Secondary Batteries: Magnesium and Beyond. *Chem. Rev.* **2014**, *114*, 11683−11720.

(7) Duchêne, L.; Remhof, A.; Hagemann, H.; Battaglia, C. Status and Prospects of Hydroborate Electrolytes for All-Solid-State Batteries. *Energy Storage Mater.* **2020**, *25*, 782−794.

(8) El Kharbachi, A.; Pinatel, E.; Nuta, I.; Baricco, M. A Thermodynamic Assessment of $LiBH_4$. *Calphad* **2012**, *39*, 80−90.

(9) Matsuo, M.; Nakamori, Y.; Orimo, S.-i.; Maekawa, H.; Takamura, H. Lithium Superionic Conduction in Lithium Borohydride Accompanied by Structural Transition. *Appl. Phys. Lett.* **2007**, *91*, 224103.

(10) Gulino, V.; Brighi, M.; Dematteis, E. M.; Murgia, F.; Nervi, C.; Černý, R.; Baricco, M. Phase Stability and Fast Ion Conductivity in the Hexagonal $LiBH_4$-LiBr-LiCl Solid Solution. *Chem. Mater.* **2019**, *31*, 5133−5144.

(11) Asakura, R.; Duchêne, L.; Kühnel, R.-S.; Remhof, A.; Hagemann, H.; Battaglia, C. Electrochemical Oxidative Stability of Hydroborate-Based Solid-State Electrolytes. *ACS Appl. Energy Mater.* **2019**, *2*, 6924−6930.

(12) Matsuo, M.; Oguchi, H.; Maekawa, H.; Takamura, H.; Orimo, S.; Volume, M. M. Complex Hydrides: A New Category of Solid-State Lithium Fast-Ion Conductors. *Mater. Matters* **2011**, *5*, 5−13.

(13) Sveinbjörnsson, D.; Myrdal, J. S. G.; Blanchard, D.; Bentzen, J. J.; Hirata, T.; Mogensen, M. B.; Norby, P.; Orimo, S.; Vegge, T. Effect of Heat Treatment on the Lithium Ion Conduction of the $LiBH_4$−LiI Solid Solution. *J. Phys. Chem. C* **2013**, *117*, 3249−3257.

(14) Unemoto, A.; Chen, C.; Wang, Z.; Matsuo, M.; Ikeshoji, T.; Orimo, S.-i. Pseudo-Binary Electrolyte, $LiBH_4$-LiCl, for Bulk-Type All-Solid-State Lithium-Sulfur Battery. *Nanotechnology* **2015**, *26*, 254001.

(15) Matsuo, M.; Remhof, A.; Martelli, P.; Caputo, R.; Ernst, M.; Miura, Y.; Sato, T.; Oguchi, H.; Maekawa, H.; Takamura, H.; Borgschulte, A.; Züttel, A.; Orimo, S.-i. Complex Hydrides with $(BH_4)^-$and $(NH_2)^-$Anions as New Lithium Fast-Ion Conductors. *J. Am. Chem. Soc.* **2009**, *131*, 16389−16391.

(16) Wolczyk, A.; Paik, B.; Sato, T.; Nervi, C.; Brighi, M.; GharibDoust, S. P.; Chierotti, M.; Matsuo, M.; Li, G.; Gobetto, R.; Jensen, T. R.; Černý, R.; Orimo, S.-i.; Baricco, M. $Li_5(BH_4)_3NH$: Lithium-Rich Mixed Anion Complex Hydride. *J. Phys. Chem. C* **2017**, *121*, 11069−11075.

(17) Zhu, M.; Pang, Y.; Lu, F.; Shi, X.; Yang, J.; Zheng, S. In Situ Formed Li-B-H Complex with High Li-Ion Conductivity as a Potential Solid Electrolyte for Li Batteries. *ACS Appl. Mater. Interfaces* **2019**, *11*, 14136−14141.

(18) Fichtner, M. Nanoconfinement Effects in Energy Storage Materials. *Phys. Chem. Chem. Phys.* **2011**, *13*, 21186.

(19) Choi, Y. S.; Lee, Y.-S.; Oh, K. H.; Cho, Y. W. Interface-Enhanced Li Ion Conduction in a $LiBH_4$−SiO_2 Solid Electrolyte. *Phys. Chem. Chem. Phys.* **2016**, *18*, 22540−22547.

(20) Blanchard, D.; Nale, A.; Sveinbjörnsson, D.; Eggenhuisen, T. M.; Verkuijlen, M. H. W.; Suwarno; Vegge, T.; Kentgens, A. P. M.; de Jongh, P. E. Nanoconfined $LiBH_4$ as a Fast Lithium Ion Conductor. *Adv. Funct. Mater.* **2015**, *25*, 184−192.

(21) Suwarno; Ngene, P.; Nale, A.; Eggenhuisen, T. M.; Oschatz, M.; Embs, J. P.; Remhof, A.; De Jongh, P. E. Confinement Effects for Lithium Borohydride: Comparing Silica and Carbon Scaffolds. *J. Phys. Chem. C* **2017**, *121*, 4197−4205.

(22) Lefevr, J.; Cervini, L.; Griffin, J. M.; Blanchard, D. Lithium Conductivity and Ions Dynamics in $LiBH_4/SiO_2$ Solid Electrolytes Studied by Solid-State NMR and Quasi-Elastic Neutron Scattering and Applied in Lithium-Sulfur Batteries. *J. Phys. Chem. C* **2018**, *122*, 15264−15275.

(23) Lambregts, S. F. H.; van Eck, E. R. H.; Suwarno; Ngene, P.; de Jongh, P. E.; Kentgens, A. P. M. Phase Behavior and Ion Dynamics of Nanoconfined $LiBH_4$ in Silica. *J. Phys. Chem. C* **2019**, *123*, 25559−25569.

(24) Breuer, S.; Pregartner, V.; Lunghammer, S.; Wilkening, H. M. R. Dispersed Solid Conductors: Fast Interfacial Li-Ion Dynamics in Nanostructured LiF and LiF:γ-Al_2O_3 Composites. *J. Phys. Chem. C* **2019**, *123*, 5222−5230.

(25) Epp, V.; Wilkening, M. Motion of Li^+ in Nanoengineered $LiBH_4$ and $LiBH_4$:Al_2O_3 Comparison with the Microcrystalline Form. *ChemPhysChem* **2013**, *14*, 3706−3713.

(26) Gulino, V.; Barberis, L.; Ngene, P.; Baricco, M.; de Jongh, P. E. Enhancing Li-Ion Conductivity in $LiBH_4$-Based Solid Electrolytes by Adding Various Nanosized Oxides. *ACS Appl. Energy Mater.* **2020**, *3*, 4941−4948.

(27) Liu, Z.; Xiang, M.; Zhang, Y.; Shao, H.; Zhu, Y.; Guo, X.; Li, L.; Wang, H.; Liu, W. Lithium migration pathways at the composite interface of $LiBH_4$ and two-dimensional MoS_2 enabling superior ionic conductivity at room temperature. *Phys. Chem. Chem. Phys.* **2020**, *22*, 4096−4105.

(28) Latroche, M.; Blanchard, D.; Cuevas, F.; El Kharbachi, A.; Hauback, B. C.; Jensen, T. R.; de Jongh, P. E.; Kim, S.; Nazer, N. S.; Ngene, P.; Orimo, S.-i.; Ravnsbæk, D. B.; Yartys, V. A. Full-Cell Hydride-Based Solid-State Li Batteries for Energy Storage. *Int. J. Hydrogen Energy* **2019**, *44*, 7875−7887.

(29) Unemoto, A.; Ikeshoji, T.; Yasaku, S.; Matsuo, M.; Stavila, V.; Udovic, T. J.; Orimo, S.-i. Stable Interface Formation between TiS_2 and $LiBH_4$ in Bulk-Type All-Solid-State Lithium Batteries. *Chem. Mater.* **2015**, *27*, 5407−5416.

(30) Unemoto, A.; Yasaku, S.; Nogami, G.; Tazawa, M.; Taniguchi, M.; Matsuo, M.; Ikeshoji, T.; Orimo, S.-i. Development of bulk-type all-solid-state lithium-sulfur battery using $LiBH_4$ electrolyte. *Appl. Phys. Lett.* **2014**, *105*, 083901.

(31) Unemoto, A.; Wu, H.; Udovic, T. J.; Matsuo, M.; Ikeshoji, T.; Orimo, S.-i. Fast Lithium-Ionic Conduction in a New Complex

Hydride−Sulphide Crystalline Phase. *Chem. Commun.* **2016**, *52*, 564−566.
(32) Das, S.; Ngene, P.; Norby, P.; Vegge, T.; de Jongh, P. E.; Blanchard, D. All-Solid-State Lithium-Sulfur Battery Based on a Nanoconfined $LiBH_4$ Electrolyte. *J. Electrochem. Soc.* **2016**, *163*, A2029−A2034.
(33) Dimitrov, V.; Sakka, S. Electronic Oxide Polarizability and Optical Basicity of Simple OxidesElectronic oxide polarizability and optical basicity of simple oxides. I. *J. Appl. Physiol.* **1996**, *79*, 1736−1740.
(34) Brunauer, S.; Emmett, P. H.; Teller, E. Adsorption of Gases in Multimolecular Layers. *J. Am. Chem. Soc.* **1938**, *60*, 309−319.
(35) Boukamp, B. Electrochemical Impedance Spectroscopy in Solid State Ionics: Recent Advances. *Solid State Ionics* **2004**, *169*, 65−73.
(36) Boukamp, B. A Package for Impedance/Admittance Data Analysis. *Solid State Ionics* **1986**, *18−19*, 136−140.
(37) Verkuijlen, M. H. W.; Ngene, P.; de Kort, D. W.; Barré, C.; Nale, A.; van Eck, E. R. H.; van Bentum, P. J. M.; de Jongh, P. E.; Kentgens, A. P. M. Nanoconfined $LiBH_4$ and Enhanced Mobility of Li^+ and BH_4^- Studied by Solid-State NMR. *J. Phys. Chem. C* **2012**, *116*, 22169−22178.
(38) Duchêne, L.; Lunghammer, S.; Burankova, T.; Liao, W.-C.; Embs, J. P.; Copéret, C.; Wilkening, H. M. R.; Remhof, A.; Hagemann, H.; Battaglia, C. Ionic Conduction Mechanism in the $Na_2(B_{12}H_{12})_{0.5}(B_{10}H_{10})_{0.5}$ closo-Borate Solid-State Electrolyte: Interplay of Disorder and Ion-Ion Interactions. *Chem. Mater.* **2019**, *31*, 3449−3460.
(39) Okada, Y.; Ikeda, M.; Aniya, M. Non-Arrhenius Ionic Conductivity in Solid Electrolytes: A Theoretical Model and Its Relation with the Bonding Nature. *Solid State Ionics* **2015**, *281*, 43−48.
(40) Zettl, R.; Gombotz, M.; Clarkson, D.; Greenbaum, S. G.; Ngene, P.; de Jongh, P. E.; Wilkening, H. M. R. Li-Ion Diffusion in Nanoconfined $LiBH_4$-LiI/Al_2O_3: From 2D Bulk Transport to 3D Long-Range Interfacial Dynamics. *ACS Appl. Mater. Interfaces* **2020**, *12*, 38570−38583.
(41) Gulino, V.; Wolczyk, A.; Golov, A. A.; Eremin, R. A.; Palumbo, M.; Nervi, C.; Blatov, V. A.; Proserpio, D. M.; Baricco, M. Combined DFT and Geometrical−Topological Analysis of Li-Ion Conductivity in Complex Hydrides. *Inorg. Chem. Front.* **2020**, *7*, 3115−3125.
(42) Zhao, W.; Yi, J.; He, P.; Zhou, H. Solid-State Electrolytes for Lithium-Ion Batteries: Fundamentals, Challenges and Perspectives. *Electrochem. Energy Rev.* **2019**, *2*, 574−605.
(43) Han, F.; Zhu, Y.; He, X.; Mo, Y.; Wang, C. Electrochemical Stability of $Li_{10}GeP_2S_{12}$ and $Li_7La_3Zr_2O_{12}$ Solid Electrolytes. **2016**, *6*, 1501590. DOI: DOI: 10.1002/aenm.201501590.
(44) Brighi, M.; Murgia, F.; Łodziana, Z.; Schouwink, P.; Wołczyk, A.; Cerny, R. Carba-Hydroborate as a Room Temperature Na-Ion Solid Electrolyte. *J. Power Sources* **2018**, *404*, 7−12.
(45) Kisu, K.; Kim, S.; Oguchi, H.; Toyama, N.; Orimo, S.-i. Interfacial Stability between $LiBH_4$-Based Complex Hydride Solid Electrolytes and Li Metal Anode for All-Solid-State Li Batteries. *J. Power Sources* **2019**, *436*, 226821.
(46) Kim, S.; Oguchi, H.; Toyama, N.; Sato, T.; Takagi, S.; Otomo, T.; Arunkumar, D.; Kuwata, N.; Kawamura, J.; Orimo, S.-i. A Complex Hydride Lithium Superionic Conductor for High-Energy-Density All-Solid-State Lithium Metal Batteries. *Nat. Commun.* **2019**, *10*, 1081.
(47) Sakamoto, J. More Pressure Needed. *Nat. Energy* **2019**, *4*, 827−828.
(48) Wang, M. J.; Choudhury, R.; Sakamoto, J. Characterizing the Li-Solid-Electrolyte Interface Dynamics as a Function of Stack Pressure and Current Density. *Joule* **2019**, *3*, 2165−2178.
(49) Sharafi, A.; Meyer, H. M.; Nanda, J.; Wolfenstine, J.; Sakamoto, J. Characterizing the Li−$Li_7La_3Zr_2O_{12}$ Interface Stability and Kinetics as a Function of Temperature and Current Density. *J. Power Sources* **2016**, *302*, 135−139.
(50) Kasemchainan, J.; Zekoll, S.; Spencer Jolly, D.; Ning, Z.; Hartley, G. O.; Marrow, J.; Bruce, P. G. Critical Stripping Current Leads to Dendrite Formation on Plating in Lithium Anode Solid Electrolyte Cells. *Nat. Mater.* **2019**, *18*, 1105−1111.
(51) Dahn, J.; Haering, R. R. Lithium Intercalation in TiS_2. *Mater. Res. Bull.* **1979**, *14*, 1259−1262.
(52) Dahn, J. R.; McKinnon, W. R.; Haering, R. R.; Buyers, W. J. L.; Powell, B. M. Structure determination of Li_xTiS_2 by neutron diffraction. *Can. J. Phys.* **1980**, *58*, 207−213.
(53) Yan, Y.; Rentsch, D.; Battaglia, C.; Remhof, A. Synthesis, Stability and Li-Ion Mobility of Nanoconfined $Li_2B_{12}H_{12}$. *Dalton Trans.* **2017**, *46*, 12434−12437.
(54) Krauskopf, T.; Hartmann, H.; Zeier, W. G.; Janek, J. Toward a Fundamental Understanding of the Lithium Metal Anode in Solid-State Batteries-An Electrochemo-Mechanical Study on the Garnet-Type Solid Electrolyte $Li_{6.25}Al_{0.25}La_3Zr_2O_{12}$. *ACS Appl. Mater. Interfaces* **2019**, *11*, 14463−14477.
(55) Krauskopf, T.; Mogwitz, B.; Rosenbach, C.; Zeier, W. G.; Janek, J. Diffusion Limitation of Lithium Metal and Li-Mg Alloy Anodes on LLZO Type Solid Electrolytes as a Function of Temperature and Pressure. *Adv. Energy Mater.* **2019**, *9*, 1902568.
(56) Rodrigues, M.-T. F.; Sayed, F. N.; Gullapalli, H.; Ajayan, P. M. High-Temperature Solid Electrolyte Interphases (SEI) in Graphite Electrodes. *J. Power Sources* **2018**, *381*, 107−115.
(57) Bruce, P. G.; Freunberger, S. A.; Hardwick, L. J.; Tarascon, J.-M. Li-O_2 and Li-S batteries with high energy storage. *Nat. Mater.* **2012**, *11*, 19−29.
(58) Murgia, F.; Brighi, M.; Černý, R. Room-Temperature-Operating Na Solid-State Battery with Complex Hydride as Electrolyte. *Electrochem. Commun.* **2019**, *106*, 106534.
(59) Duchêne, L.; Kim, D. H.; Song, Y. B.; Jun, S.; Moury, R.; Remhof, A.; Hagemann, H.; Jung, Y. S.; Battaglia, C. Crystallization of Closo-Borate Electrolytes from Solution Enabling Infiltration into Slurry-Casted Porous Electrodes for All-Solid-State Batteries. *Energy Storage Mater.* **2020**, *26*, 543−549.
(60) Doux, J. M.; Nguyen, H.; Tan, D. H. S.; Banerjee, A.; Wang, X.; Wu, E. A.; Jo, C.; Yang, H.; Meng, Y. S. Stack Pressure Considerations for Room-Temperature All-Solid-State Lithium Metal Batteries. *Adv. Energy Mater.* **2020**, *10*, 1903253.
(61) Sendek, A. D.; Cheon, G.; Pasta, M.; Reed, E. J. Quantifying the Search for Solid Li-Ion Electrolyte Materials by Anion: A Data-Driven Perspective. *J. Phys. Chem. C* **2020**, *124*, 8067−8079.
(62) McCloskey, B. D. Attainable Gravimetric and Volumetric Energy Density of Li-S and Li Ion Battery Cells with Solid Separator-Protected Li Metal Anodes. *J. Phys. Chem. Lett.* **2015**, *6*, 4581−4588.

https://dx.doi.org/10.1021/acsaem.0c02525
ACS Appl. Energy Mater. 2021, 4, 1228−1236